Experimental validation of the seismic analysis methodology for free-standing spent fuel racks

Abstract

Spent fuel racks are steel structures used in the storage of the spent fuel removed from the nuclear power reactor. Rack units are submerged in the depths of the spent fuel pool to keep the fuel cool. Their free-standing design isolates their bases from the pool floor reducing structural stresses in case of seismic event. However, these singular features complicate their seismic analysis which involves a transient dynamic response with geometrical nonlinearities and fluid-structure interactions. An accurate estimation of the response is essential to achieve a safe pool layout and a reliable structural design. An analysis methodology based on the hydrodynamic mass concept and implicit integration algorithms was developed ad-hoc, but some dispersion of results still remains. In order to validate the analysis methodology, vibration tests are carried out on a reduced scale mock-up of a 2-rack system. The two rack mockups are submerged in free-standing conditions inside a rigid pool tank loaded with fake fuel assemblies and subjected to accelerations on a unidirectional shaking table. This article compares the experimental data with the numerical outputs of a finite element model built in ANSYS Mechanical. The in-phase motion of both units is highlighted and the water coupling effect is detailed. Results show a good agreement validating the methodology.

KEY WORDS: Vibration tests; Free-standing; Rack; Water coupling, hydrodynamic mass.

1 Introduction to the rack seismic problem

Racks are metallic structures formed by a rigid pedestal and an array of rectangular parallelepiped storage cells. Rack units rest submerged in free-standing conditions on the depths of the spent fuel pool and spaced by only a few centimeters. The minimal clearance space in between is actually limited by the potential collisions during an earthquake event. Seismic accelerations are actually transmitted from the pool to the rack units though friction on supports and compression of the water volume. Hence, each base-isolated rack undergoes a complex 3D motion relative to the pool including sliding, rocking, twisting and turning. Moreover, fuel assemblies are free to rattle inside their storage cell hitting the cell walls and affecting the motion of the units. It is anticipated that both motions involve inertial and viscous forces as well as fluid-structure interactions.

The rack seismic response is extremely difficult to predict given the uncertainties associated with inertial forces, geometrical nonlinearities and fluid-structure interactions. However, an accurate estimation of this response is essential to achieve a safe pool layout and a reliable structural design. Hence, the United States Nuclear Regulatory Commission has issued overall design requirements and licensing acceptance criteria for their performance (USNRC, 1979, 1981). In parallel, an ad-hoc analysis methodology has been developed to overcome these difficulties in a cost-effective way (De Grassi, 1992). It uses finite element models to conduct an implicit transient analysis across the seismic event. Such numerical models use dynamic contacts to delimit the motion boundaries and simulate the associated impact forces and friction effects. Moreover, they take advantage of the hydrodynamic mass concept (Fritz, 1972; Chung and Chen, 1976) to approach the fluid-structure interaction and simulate the water coupling (Soler and Singh, 1982, 1984). However, the numerical outputs are highly sensitive to a number of variables and some dispersion of results still remains. This uncertainty not only comes from the input data, but also from the assumed modelling properties and the user-defined solution controls (Merino et al., 2017). Experimental test are

carried out on a scaled 2-rack mock-up equipped with fake fuel dummies in order to validate the modelling and analysis procedures.

2 Experimental vibration tests

2.1 2-rack physical model

A vibration tests campaign is carried out by a Spanish joint collaboration between Instituto de Hidraulica de Cantabria and Equipos Nucelares S.A. (ANSTER, 2015). It aims to enlarge the previous experimental studies on isolated racks (Fujita et al., 1988 and 1990; Moudrik et al., 1995; Queval et al., 1999; Iwasaki et al., 2012a; Kaneko and Shirai, 2015; Shakamoto et al., 2017; Liu at al., 2018) by focusing on the interaction between more than one unit. Hence, a physical 2-racks model representing a portion of a real spent fuel is built and tested on a unidirectional vibration table. It represents a typical rack geometry with an ordinary slenderness ration in an arrangement with common clearance spaces.

Figure 1 shows the whole physical model that includes a vibration table, a pool tank and two rack mockups and loaded with fuel dummies. For economic and practical reasons, the physical model is designed to the scale 1/3 in order to reduce its size and mass. Then, all geometric dimensions are multiplied by 1/3, time is compressed by 1/√3 and masses are lightened by the factor 1/3^2. Such a similarity law respects both accelerations and densities and avoids problems related to scaling gravitational effects and materials densities. The rest of physical dimensions defining the model can be derived from these three fundamental similarities.

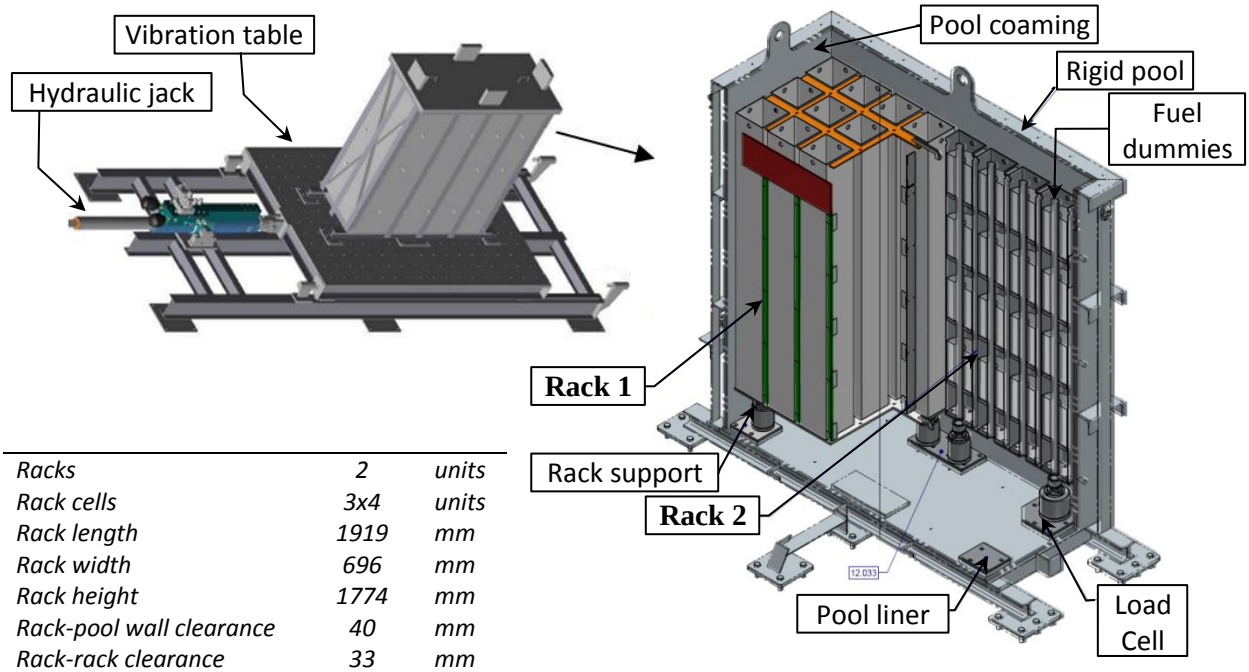

Racks	*2*	*units*
Rack cells	*3x4*	*units*
Rack length	*1919*	*mm*
Rack width	*696*	*mm*
Rack height	*1774*	*mm*
Rack-pool wall clearance	*40*	*mm*
Rack-rack clearance	*33*	*mm*

Figure 1. Sketch of the vibration table and the rack mock-ups inside the testing tank

The vibration table is equipped with a hydraulic jack able to excite 10tons at 1g at the required frequency and amplitude. Pool walls and supports are heavily reinforced to increase their rigidity and to avoid any resonance during the shakings. The ensemble table-tank is therefore considered as a rigid body. The rack mock-ups are free-standing and allowed to move on their own. Their base-isolation is achieved through pad supports sliding over a metallic liner in the tank floor. Each mock-up is equipped with 4x3 squared cells containing 12 fuel dummies. Fuel dummies are made by a tubular bar with attached dead-weights at four levels in order to replicate the original natural frequencies.

It is noted here that the spent fuel pools are deep enough to differentiate between impulsive and convective regions (Housner, 1963). Rack units are located in the impulsive region where the water volume moves in unison with the tank, far enough from the influence of the convective component of the surface. Hence, the testing tank only

represents the lower volume of the real pool. However, in order to ensure a good representation of the physical phenomena, the testing pool needs to be covered to avoid head loses associated to sloshing at the free surface. The role of the cover is not to replace pressure of the water head but just to set an effective upper boundary that confines the water volume. The cover leaves a 35cm sheet of water over the rack units, which for the given pool dimensions is considered thick enough to simulate the 3D flow disturbances due to the bending of the streamlines around the racks edges. Recent simulations with Computed Fluid Dynamics software confirm the limited influence of surface sloshing (Tataki et al., 2017).

The physical model is designed to test different configurations. The natural frequencies of the rack mock-ups can be adapted through stiffness-control devices on supports. The friction coefficient between rack supports and pool liner is selected trough interchangeable plates of different rugosity. The gap exiting between the fuel dummies and the cell wall can be modified through retractable screws. The most representative variables of the testing configurations are provided in Table 1.

Table 1 Variables defining the testing configuration

Variables	*Units*	*Value*	**Source**
Seismic accelerogram	m/s^2	Fig.7.3	Measured from AC1
Rack unit mass	kg	500	Weighed as built
Fuel loading mass	kg	1900	Weighed as built
Horizontal Eigen-frequency	Hz	16	Hammer impact test
Vertical Eigen-frequency	Hz	90	FE Analysis
Rack-Pool friction coefficient	-	0.25	Measured in an inclined angle
Fuel-Cell gap space	mm	6.40	As per design
Fuel beam sectional inertia	m^4	8.25 E-8	As per design

2.2 Data acquisition system

Experimental data are collected by multiple sensors placed at different locations all over the pool. Figure 2 represents a pool section along the symmetric XY plane to illustrate their location.

- An accelerometer (AC1) is boarded on the vibration table to track the acceleration time-history of the shaking table in x direction,
- A load cell (LC1) is placed at the contact between the rack support and the pool floor. It measures the vertical reaction along the test,
- Pressure sensors (PS1-PS7) record the hydrodynamic pressures at different locations on the rack sides as well as on the pool walls,
- Several video cameras (CAM) attached to the vibration table film the motion of respective targets through transparent windows on the pool walls. They return the 3D relative displacements and rotations of the rack units.

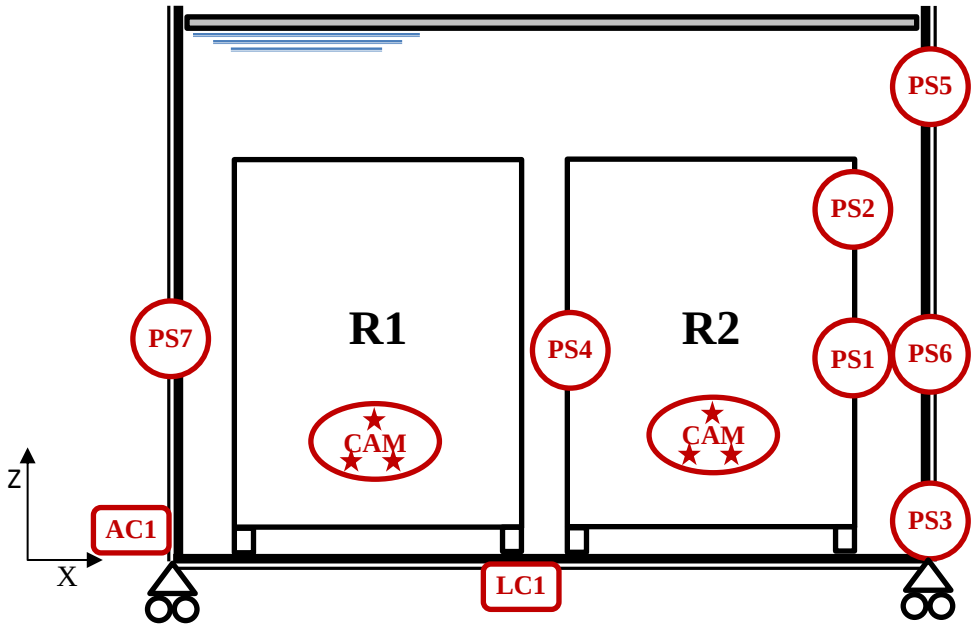

Figure 2. Instrumentation of the data acquisition system. Location of sensors.

3 Experimental results

3.1 Rack response to the seismic excitation

The physical model is vibrated in the x-direction with a synthetic earthquake derived from real design response spectra. It combines waves of different amplitude and frequency according to the Power Spectra Density method. The resulting accelerogram lasts for 10 seconds with peaks up to ±8 m/s^2 reaching velocities up to 0.7 m/s. A low excitation starting interval (0-2 seconds) is followed by high excitation shakings (2-8 seconds) which progressively blow out during the last 2 seconds. Figure 3 shows how the accelerogram drives the sliding displacement of the racks. Slidings are measured as the difference between the displacements of the pool and the rack centre along the x-axis. The peaks of the sliding cycles are in phase with those of the pool shakings which indicates that the pool accelerogram clearly governs the rack motion.

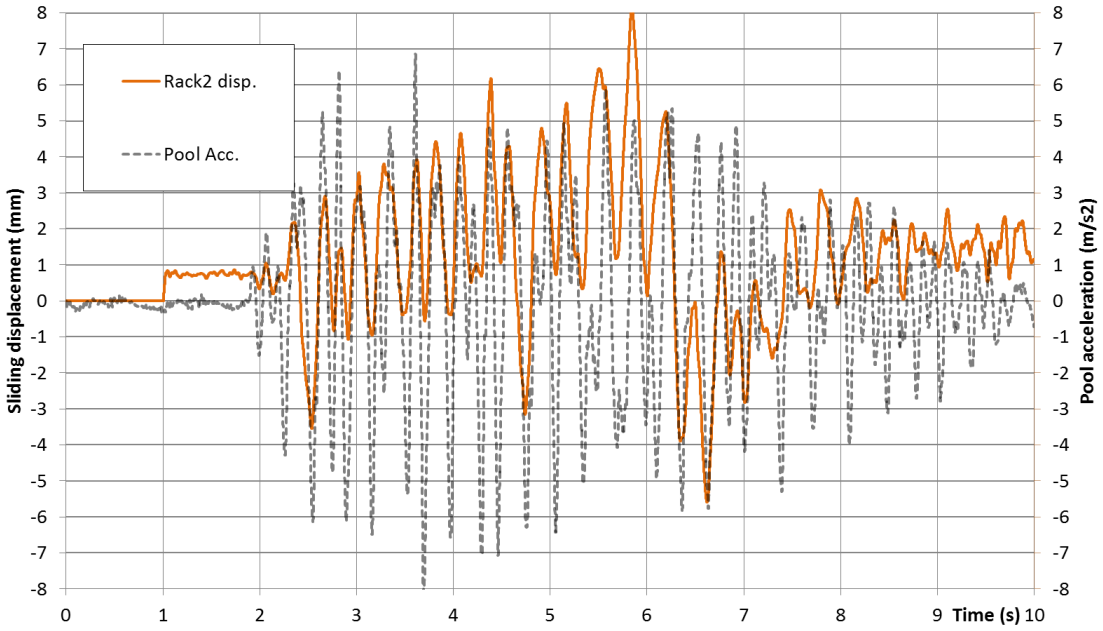

Figure 3. Relationship between the acceleration-time history and the sliding displacement of Rack2

The sliding displacements and the amplitude of the acceleration cycles are closely related. Indeed, the largest slidings occur during the interval of maximal accelerations (between t=2s and t=8s). In addition, despite the fact that

free-standing racks have no defined frequency response to seismic motion, their sliding response increases with the period of the acceleration excitation (Iwasaki et al., 2016). Both facts indicate that the governing factor of the slidings is the velocity reached by the units. All in all, the amplitude and frequency of the seismic acceleration time-history determines the energy of the excitation; large accelerations throughout long cycles give the rack units time to gain velocity. From the displacements point of view, it corresponds to high frequency and large amplitude pool displacements.

With regard to the rocking response, it is noted that rack supports tend to alternately uplift and pierce the pool liner at each rack body oscillation. Figure 4 highlights that the reaction forces on support also tend to follow the frequency of the accelerogram. The initial reaction represents the underwater self-weight supported by each of the 4 feet. This value is more than doubled during the seism as a consequence of the inertial effects and the contribution of the fuel rattling inside their storage cells. It starts at 5.88kN (i.e. the underwater self-weight) and reach 11.32kN at its peak (t=3.8s). On the other hand, it is worth noting that the support foot never lift-ups during the test. The reaction force never goes under 2kN.

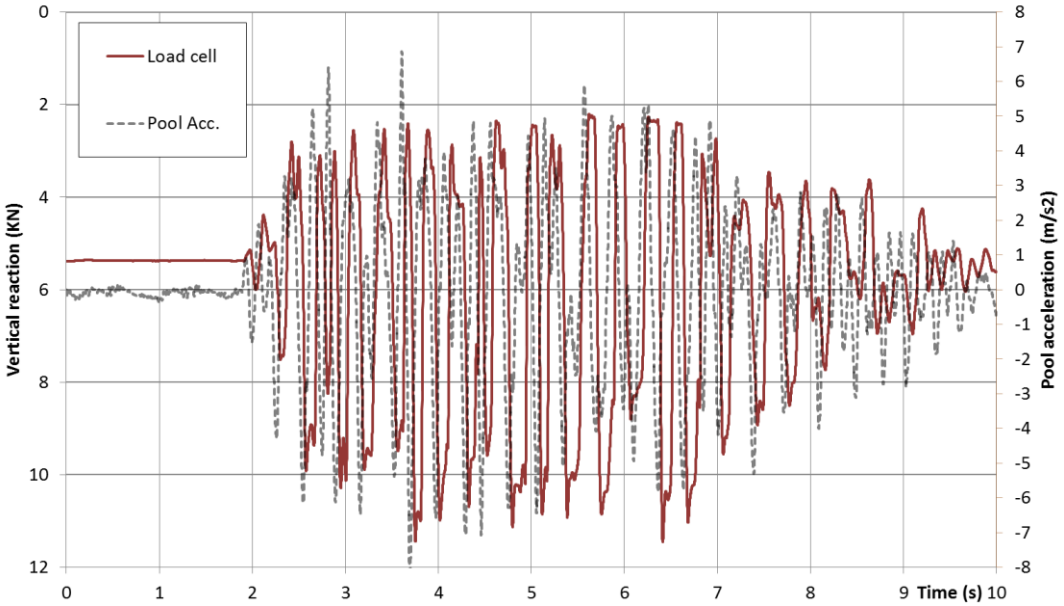

Figure 4. Relationship between the Acceleration-time history and the reaction forces on support

3.2 Water coupling

The motions of pool and racks are connected through the water volume enclosed in-between. Any relative acceleration of the submerged structures creates local compressions or decompressions in the water volume that can only be relieved by flowing through the clearance spaces towards a new accommodation. Hence, the degree of water coupling is subjected to the drag coefficient of the rack body and to their arrangement within the pool. Large rack faces and the presence of outer plates boost the hydrodynamic resistance arising higher pressures. Narrow water gaps create flow bottlenecks blocking the evacuation and increasing the confinement.

The resulting pressure field tends to couple the whole system by opposing relative acceleration. Together with the friction forces, it transmits the seismic accelerations from the pool walls to the rack faces. Figure 5 shows the transmission of water pressure between the middle height of the pool wall (PS6) and the centre of the rack face (PS1). Figure 6 plots the water pressure at PS1 against the accelerogram and the Rack2 slidings respectively. The pressure peaks and the acceleration peaks are aligned in synchrony. However, an out-of-phase component appears during the high excitation as a consequence of the rack sliding relative acceleration.

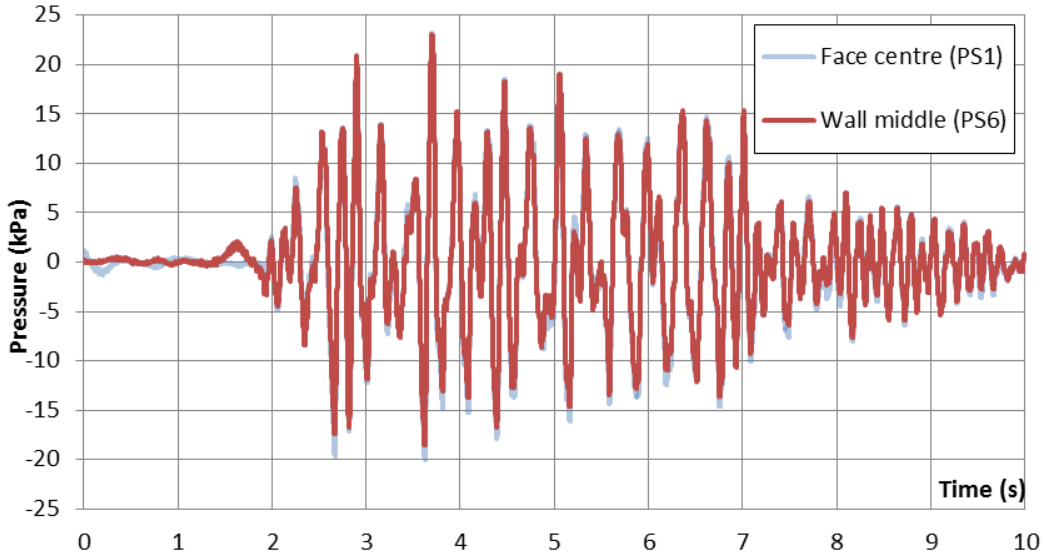

Figure 5. Coupling pressure between the pool wall and the rack face

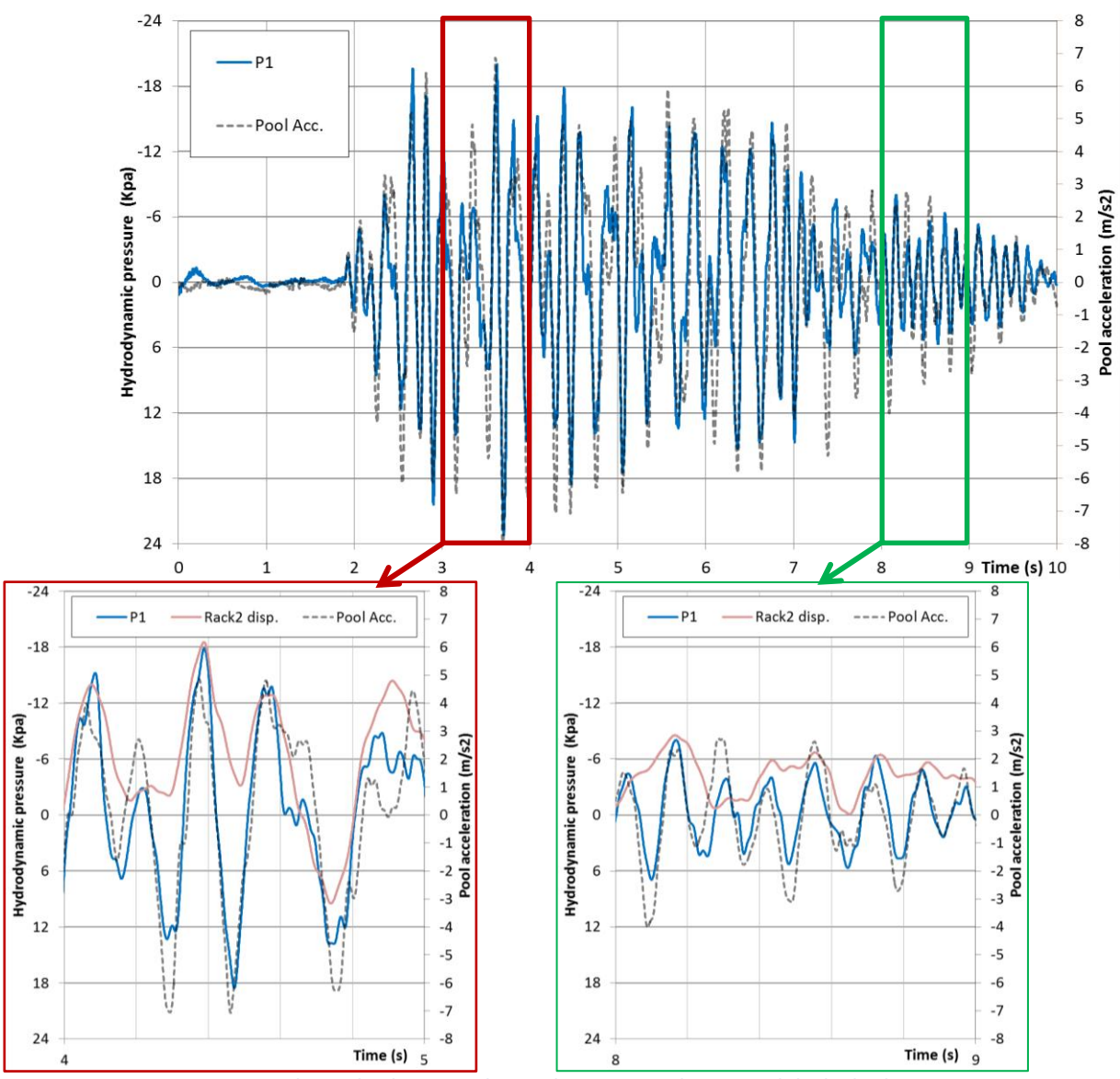

Figure 6. Relationship between the acceleration-time history and the hydrodynamic pressures

However, the water action is not uniform. Rack faces act as blunt bodies blocking the pressure field with a high angle of attack. Streamlines have to bend around the edges looking for a way out through the clearance spaces to relief the pressure. This internal recirculation flow lowers down the pressure on the boundaries. This issue is noticed by the pressure sensors during the vibration test. Figure 7 provides pressure readings at the bottom, middle height and top of the pool wall. In the same way, Figure 8 points out up to 25% difference on the pressure peaks between the

centre and the top of the rack. This pressure fall is larger on the top edge as streamlines finds an easy exit with less confinement. This observation is in agreement with previous experimental test carried out in Japan (Iwasaki et al., 2012b).

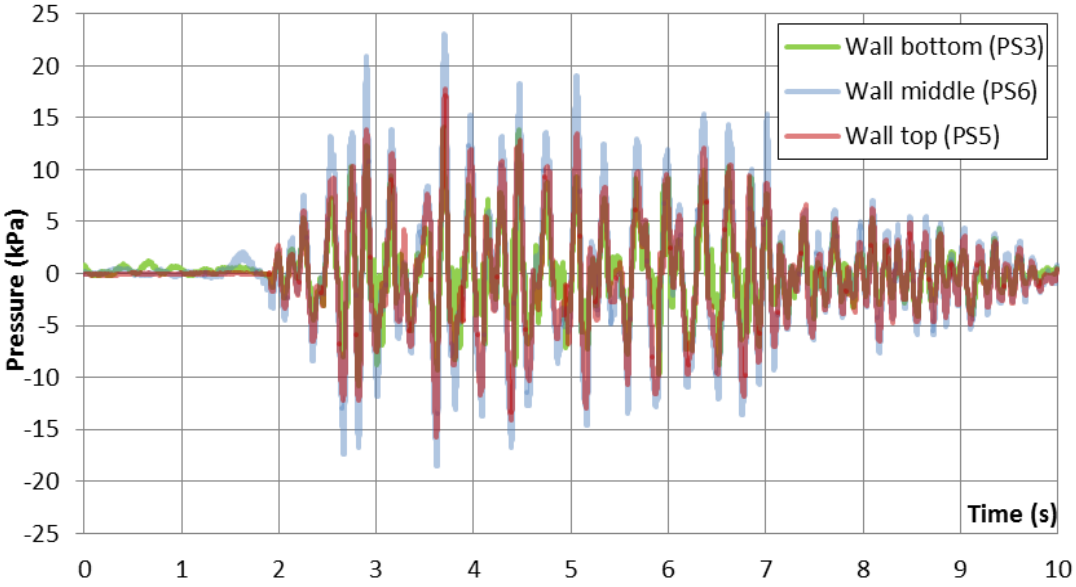

Figure 7. Boundary effects on the water pressure distribution along the pool wall

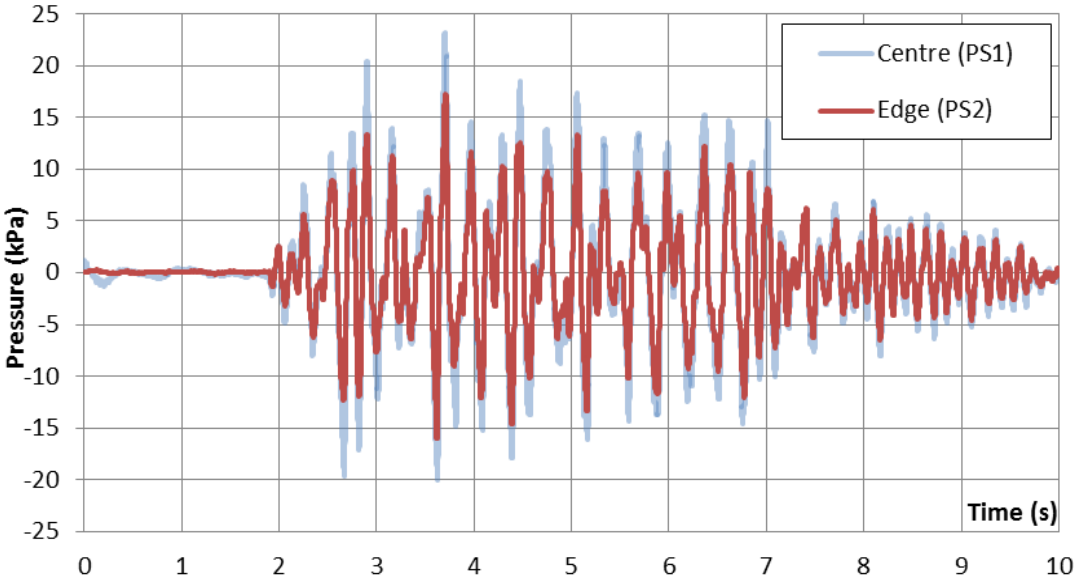

Figure 8. Boundary effects on the water pressure distribution along the rack face

3.3 In-phase motion of rack units

The aforementioned water coupling leads the 2 rack units to a nearly in-phase motion with similar amplitudes. Figure 9 plots the sliding displacements of both units along the x-axis measured as the difference between the displacements of their centres of masses with respect to the pool. Positive or negative slidings represents approximations to the right or left pool walls respectively. The differences in the sliding paths of both units highlight how their separation progressively cumulates along time from its initial gap (t=0) to the 8 mm at the end of the earthquake (t=10).

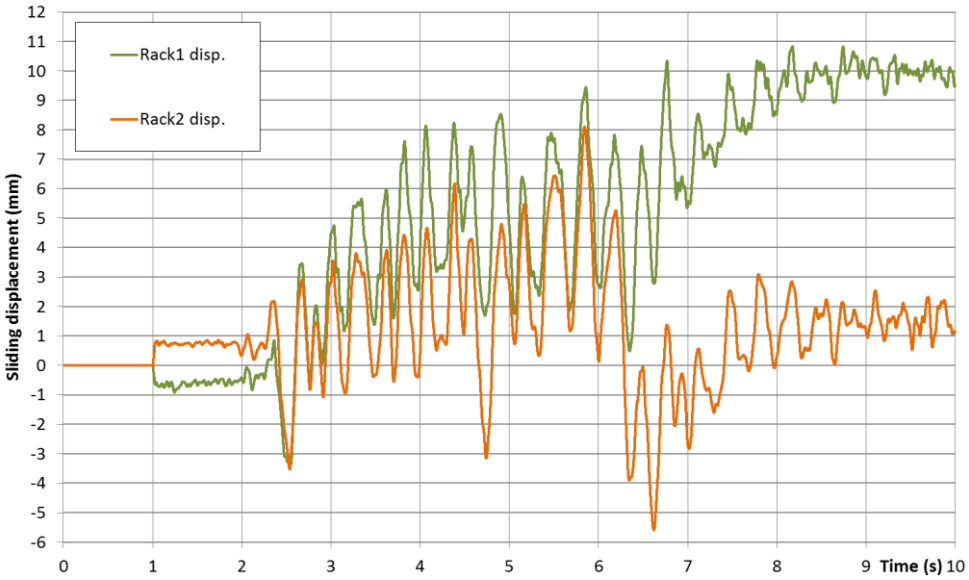

Figure 9. Sliding displacements of both rack units

Figure 10 compares the internal pressure in-between rack units to the external pressure between rack and pool. Water pressure is clearly larger at the outskirts of the pool. A factor 5 is noticed between both. It confirms the small alteration of the water gaps in-between racks and therefore a nearly in-phase motion.

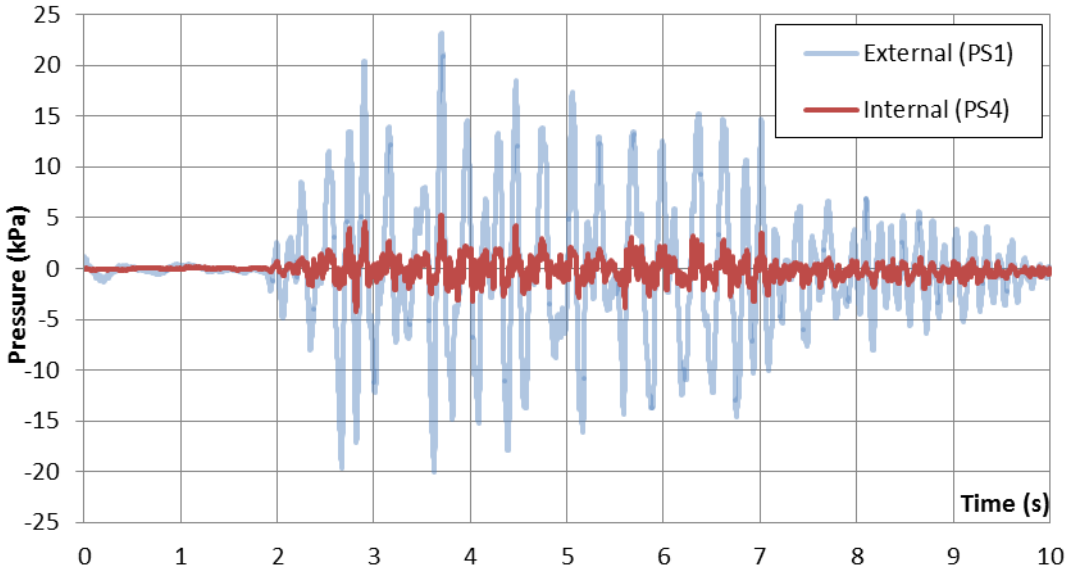

Figure 10. Comparison between internal and external water pressures

4 Numerical analysis

4.1 Finite element model

The finite element model showed on Figure 11 is built in ANSYS Mechanical 14 (ANSYS, 2013) in agreement with the notice QA2012-01. It simulates the sliding and rocking motion of the aforementioned 2-rack vibration test by allowing 3D spatial displacements and rotations. The number of nodes and elements is reduced as much as possible in order to limit the computational cost. Mechanical properties are assigned to these finite elements to replicate the natural frequencies and achieve realistic simulations of the physical of the system.

Rack structures are shaped through beam elements (ANSYS BEAM188) and lumped masses (ANSYS MASS21). The pool is considered to be an infinitely rigid solid and therefore modelled by a unique node. Rack units are formed by a rigid 4-support pedestal and a vertical cantilever body beam representing the storage cells. The ensemble of fuel assemblies are assumed to oscillate in phase so they represented by a unique fuel beam. Both beams are initially

collinear centred at the vertical axis and separated by a constant gap along the rack height. They are connected at multiple levels through cylindrical contacts and dynamic fluid coupling elements. The rack and fuel self-weights are applied as a vertical force on their centroid whereas the ground seismic loading is directly enforced to the pool as an acceleration-time history to the pool (ANSYS, 2012).

Dynamic contacts (ANSYS CONTA178) set the motion boundaries and simulate the impacts and frictions raised between rack supports and pool floor as well as between fuel and cells. Hydrodynamic couplings replace the water action by added masses. ANSYS MATRIX27 elements connect racks and pool to specify the previously-computed added masses. The resulting coupling forces are spread over the whole rack surface. Similarly, ANSYS FLUID38 elements connect the fuel assemblies and the rack body beam to specify the hydrodynamic coupling brought by the water volume trapped in the annular gap of the storage cell.

Different approaches to such a conceptual model have been developed and used for design purposes (Habedank et al., 1979; Ashar and DeGrassi, 1989; Zhao et al., 1996; Zhao 1997; Lee et al., 1998; Hinderks et al., 2000; Champomier et al. 2001; Iwasaki et al. 2012c, 2013; Liu et al, 2017).

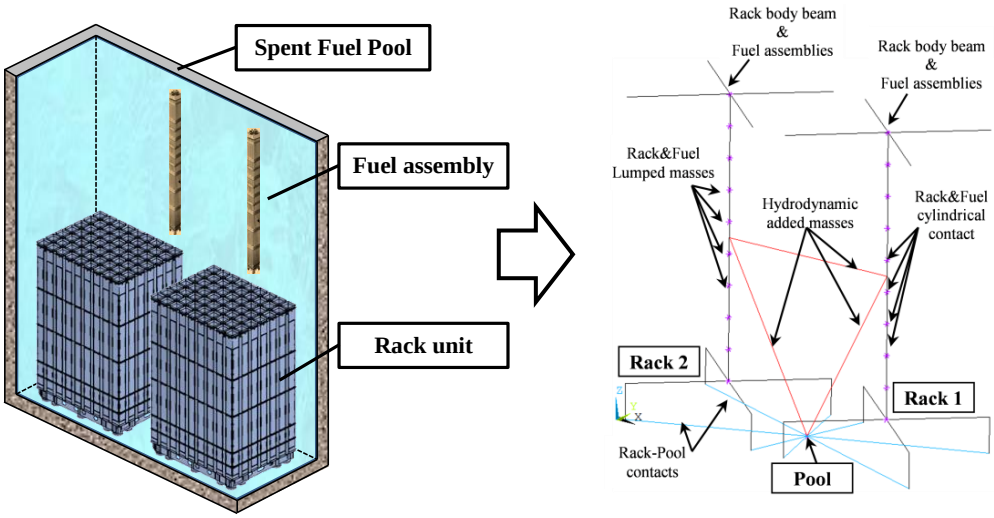

Figure 11. Finite Element model for transient seismic analysis

4.1.1 Dynamic contact elements

Rack units experience two types of contacts during their seismic response. Firstly, the rack oscillations around their vertical position affect the vertical reaction force at the contacts between rack supports and pool floor. Such a rocking response leads to alternative uplift and penetration events. Secondly, the rattling motion of fuel assemblies inside their storage cells arises multiple impacts along the cell walls. Their occurrence is subjected to the relative motion between fuel and rack and to the hydrodynamic coupling of the water volume enclosed within both.

These contacts are generally assumed elastic whit enforced energy conservation. They are modelled as compression-only spring elements following the penalty-based method. It authorizes slight penetrations between interfaces in order to mitigate the stiffness discontinuity and to facilitate the analysis convergence. However, it artificially softens the impacts and increases their duration affecting the energy pulse. The allocated contact stiffnesses determine the roughness of the impacts. Friction forces appear at the contact interface when the contact is closed. They are assumed proportional to the normal reaction responding to the Coulomb model. It is current practise to ignore the slight difference between static and dynamic friction in order to simplify the analysis. Its potential impact of results is considered of secondary importance in relation to the overall analysis uncertainty.

4.1.2 Hydrodynamic masses

In addition to the buoyancy force, the motion of the submerged structures is affected by fluid-structure interactions. As mentioned in Section 3.2, the hydrodynamic pressures induce a significant action over the wet surfaces that affect the dynamic response of the rack system and the stored fuel assemblies. It opposes the relative motion between wet boundaries creating a ‘water coupling effect’ that push for an in-phase motion (Champomier et al.,

1991). The magnitude of these coupling forces depends on the geometrical shape of the racks and the clearance space between units.

This fluid-structure interaction is numerically approached here through hydrodynamic masses which represent the equivalent mass of water vibrating with the in-motion structure. Thus, water coupling is no longer considered as external forces, but assimilated as a virtual extension of the structure that changes its effective mass instead. These added masses are calculated once for the initial pool layout prior to launch the analysis and then added to the mass matrix of the dynamic equation of motion (Eq. 1). Analytical formulations derived from potential theory exist for 2D and 3D approximations to a single rack (Stabel et al., 1993) with good agreement to computed fluid dynamic results (Ren and Stabel, 1999; Stabel and Ren, 2001). However, an auxiliary Finite Element model of the whole pool is used here to compute all the terms of the hydrodynamic mass matrix [m_{hydro}]. A Lapacian flow is assumed considering inviscid and incompressible water with low fluid velocities. It avoids consideration of boundary layer separation and wake formation and therefore allows the adoption of a thermal analogy with the steady-state equation of heat transfer. Figure 12 prints the colour map of pressures on the pool walls and rack faces raised by a virtual x-positive pool acceleration. Warm reddish colours represent positive pressures whereas cold bluish colours indicate negative pressures. There is no variation of pressure at the plane of symmetry.

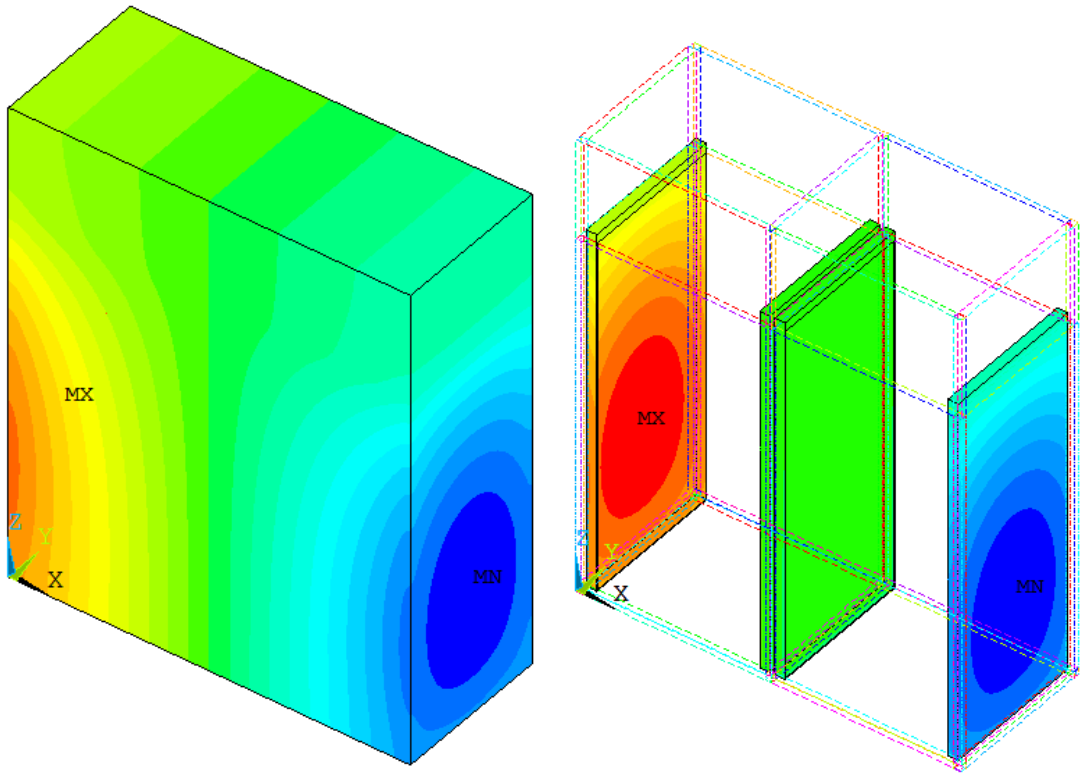

Figure 12. Distribution of pressures after virtual relative x-positive pool acceleration

The pressure field respects the symmetry of the pool along the XZ plane but it is not uniformly distributed. It follows a parabolic distribution over the rack face with an important pressure fall near the open waters at the top edge of the racks. Both maximum and minimum pressure points are located at around 1/3 of the rack's height which corresponds to the hidden areas of most difficult access. This is in agreement with the experimental findings of Figure 8. These boundary effects affect the total integral of forces and create eccentric overturning moments that must be adequately transferred to the structural model. It proves the advantage of 3D pool models with a real integration of forces face to a simplistic analytical formulation.

4.2 Transient seismic analysis

The geometrical nonlinearities raised by the dynamic contacts invalidate the application of the superposition principle. Hence, an implicit transient analysis with direct integration of the equation of motion (Eq.1) becomes unavoidable. Full equilibrium is required for every node in the 3 directions of the space. Nonlinearities are gradually

approached by iterative series of linear Newton-Raphson approximations that update the tangent stiffness matrix after each equilibrium iteration.

$$\left[M + m_{hydro}\right]\{\ddot{u}(t)\} + [C]\{\dot{u}(t)\} + [K]\{u(t)\} = \{F(t)\} \quad (1)$$

Where [*M*], [*C*] and [*K*] are the mass, damping and stiffness matrices of the structural system respectively and {u(t)}, {u̇(t)} and {ü(t)} are vectors containing the translational and rotational degrees of freedom of the structure and their respective velocities and accelerations. {F(t)} is a vector containing the time-varying forces applied at each nodal degree of freedom. It reduces to the underwater self-weight when the seismic loading is input as a pool acceleration-time history.

Hydrodynamic forces are replaced by the addition of the hydrodynamic mass matrix [m_{hydro}]. Diagonal terms represent the forces acting on rack units due to their acceleration itself. Off-diagonal terms symbolize water coupling among units. It is noted that hydrodynamic mass matrix is computed just once for the initial pool layout and kept constant across the analysis. It assumes little changes on the clearance spaces with negligible impact on the hydrodynamic masses as evidenced by the small-relative experimental displacements between racks.

Solution controls define the performance of this implicit analysis and therefore the accuracy of the outputs. They set the time scheme, the integration algorithm, the numerical solver, the Newton-Raphson (N-R) iterative procedure the convergence criterion, etc. Since theoretical studies are restricted to linear cases, solution controls have to be specified after a validation, verification and calibration process for the problem at hand.

4.2.1 Adaptive time stepping

Implicit time integration algorithms use finite difference expansions to integrate the differential equation of motion. The seism event is then discretised into short time steps where the system equilibrium is enforced. However, equilibrium across the time interval is not ensured and peak values would be unintentionally flattened. The step size becomes therefore a key parameter in the correct tracking of the response. Short enough steps remain on the linear range of the response approaching to the equilibrium of the intermediate states. On the other hand, long steps may capture nonlinear deviations requiring many N-R equilibrium iterations.

Rather than specifying a fixed step size for the entire analysis, adaptive time stepping schemes are in charge of automatically change the step size as the calculation proceeds. Such a tool increases or reduces the duration of the steps within a user-defined range to follow the peculiarities of the analysis. Hence, the software tries to solve the steps using the last known step size. The system is considered in equilibrium and the solution accepted when the residuals between internal and external forces met the convergence criterion. Whenever convergence is not fulfilled after a given number of N-R equilibrium iterations, the step is split (e.g. bisected in two halves) and the iteration process restart. This operation is repeated until the unbalanced residual becomes acceptably small and the convergence criterion is reached. Then, the N-R iterative process stops and the algorithm jumps to the next step. Hence, the maximal number of authorized N-R equilibrium iterations and the convergence tolerance influence the step size. A constrained convergence tolerance together with a low-limited number of equilibrium iterations drive to shorter steps with earlier bisections.

Adaptive time stepping suits well the specific seismic behaviour of racks as it adjusts the step size to the computation needs. It closes the step size when convergence issues are encountered (e.g. rocking behaviour with rough contacts). Then, it opens the step size for easy convergence stretches (e.g. fixed or sliding behaviour) up to reach the predefined maximal size. The maximal allowed step size specifies the upper bound of the step duration. The adaptive time stepping is not authorized to exceed this span of time. It implicitly defines the minimal number of steps to be performed throughout the transient analysis. Short steps result in a better tracking of the response, but they increase the computational time with a high marginal cost.

4.2.2 Implicit integration algorithm

The numerical integration of Equation 1 is carried out by the HHT algorithm (Hilbert et al., 1977) using a linear combination of two successive time steps. This well-known algorithm is a generalised form of the α-method derived from the original Newmark method (Newmark, 1959). It ensures second-order accuracy while reducing numerical noise. The associated integration parameters set the weighting of the interpolations in order to control the numerical damping with regard to the step size and the oscillation period of the structure. They are defined through the amplitude decay factor (γ) which should remain within in the interval (0, 1/3).

4.3 Damping model ratio

The damping model is essential to accurately simulate how rack oscillations decay during their motion. Classical viscous damping assumes this energy dissipation as directly proportional to the absolute nodal velocity, which means that both rigid solid motion and relative deformation are damped without distinction. Hence, the Rayleigh approach has become widely used due to its easy numerical implementation and mathematical conveniences. It defines the damping matrix [*C*] as a linear combination of the mass and stiffness matrices (Eq. 2).

$$[C] = \alpha[M] + \beta[K] \tag{2}$$

Where, alpha and beta are the mass and stiffness matrix proportional constants. Mass-proportional damping contributes to the diagonal terms of the damping matrix. Therefore it particularly affects the low frequency modes of vibration including the rigid solid motion. Stiffness-proportional damping fulfils non-diagonal terms, so it is able to damp relative motion and deformations. It increases linearly to the response frequency so it affects the different oscillation frequencies with different weight. The combination of both Rayleigh coefficients defines the damping ratio (ξ) as a function of the oscillation frequency according to Equation 3. Hence, only the damping ratio of a given couple of frequencies (i=2) can be accurately specified which struggle to adapt to the heterogeneous response of the rack system.

$$\xi_i = \frac{1}{2}\left(\frac{\alpha}{\omega_i} + \beta\omega_i\right) \tag{3}$$

Where ξ represents the fraction of critical damping (i.e. the quickest approach to zero amplitude) and ω refers to the angular frequency ($\omega = 2\pi f$). Since the response of the rack system is characterized by a wide spectrum of frequencies going from rigid solid motion to high frequency contact impacts, different Rayleigh coefficients should be assigned to the Finite Element elements. It is advised to damp only the structural elements leaving aside coupling elements as friction contacts and hydrodynamic coupling.

5 Comparison between experimental and numerical results

Vibration tests were repeated up to achieve valid results without collision between units or pool. In parallel, multiple numerical analyses with different modeling and analysis variables are run in counterpart in order to simulate the experiments. Finally, experimental and numerical outputs are compared in order to evaluate the overall accuracy of the analysis methodology. However, it is noted that even in closely controlled test, it is difficult to perfectly recreate the experimental observation through numerical analysis.

5.1 Calibration of the modelling and analysis variables of the finite element model

The rack seismic response certainly fluctuates with variations in load data, model properties, solution controls and damping ratios. The choice of these variables is often left to the appreciation of the engineer and requires a deep understanding of the physics of the problem (Merino et al., 2018). Hence, different sets of input variables are tested in the present investigation in order to match experimental results. The final selection of input variables resulting from this tuning process is described hereafter and listed in Table 2 for ease of reference.

- Real spent fuel pools are massive and rigid so the rack-pool contact stiffness tends to infinite. However, this pool mockup experiences some undesired deformations and rotations due to the weakness of the rail-roller

gap on the vibration table. Hence, the overall contact stiffness is softened to 1E9 N/m. It returns penetrations up to 1.5E-4 m which agrees with experimental measures.

- The stiffness of fuel-cell contact is subjected to the support conditions and flexural rigidity of the plate forming the cell. It is estimated at 1E6 N/m for a single bundle, going to 1.2E7 N/m for 12 contacts in parallel accepting the conservative assumption of in-phase motion for the fuel assemblies. However, contacts are softened to 6E6 N/m in order to realistically represent the heterogeneity of the impacts that progressively occur during a time span. It represents half of the assemblies hitting simultaneously.
- Step size is limited under 1E-4 seconds. Together with a constrained limit in the N-R iteration (only 4), it gives advantage to step bisections rather than iterations when facing nonlinearities.
- 1E-7 m is adopted as convergence tolerance criterion for the infinite norm of residual displacement vector. Such a small value ensures an accurate energy exchange during the elastic impacts.
- An amplitude decay factor of 0.1 is used in the simulations. It reduces the numerical noise but causes little impact on the outputs for the given time step.
- No alpha damping is considered. Fluid viscous damping does not affect the rack rigid solid motions as water velocities remain low (i.e. less than 1m/s)
- Beta damping is set to 2% of the critical damping at the first natural frequency (i.e. 16 Hz). It is typical for welded steel structures working stresses under ½ yield point (Stevenson J.D., 1980). However it may cause overdamping in the higher frequency modes of response affecting the vertical oscillations after rocking impacts (e.g. 40% at 80 Hz).

Table 2. Calibration of the modelling and analysis variables of the finite element model

Variables	*Units*	*Value*	**Source**
Hydrodynamic mass matrices	kg	$[m_{hydro}]$	Computed Auxiliary model
Rack-Pool contact stiffness	N/m	1.00E+09	Estimated from design
Fuel-Cell contact stiffness	N/m	6.00E+06	Estimated from design
Maximum allowed step size	s	5.00E-04	Recommendation
Number of equilibrium iterations	#	4	Recommendation
Convergence tolerance	m	1.00E-08	Recommendation
Integration parameter (HHT amplitude decay factor)	γ	0.10	Recommendation
Rayleigh stiffness-proportional damping (alpha)	-	0.00	0% at 0Hz
Rayleigh mass-proportional damping (beta)	-	4.05E-4	2% at 15.7Hz

5.2 Sliding displacements

Figures 13 and 14 compare the sliding displacements of both rack units obtained from numerical analysis and those collected from the tests. Even though some differences are found in the amplitudes, the general tendencies are quite similar. Deviations increase through the time as a result of the cumulative propagation.

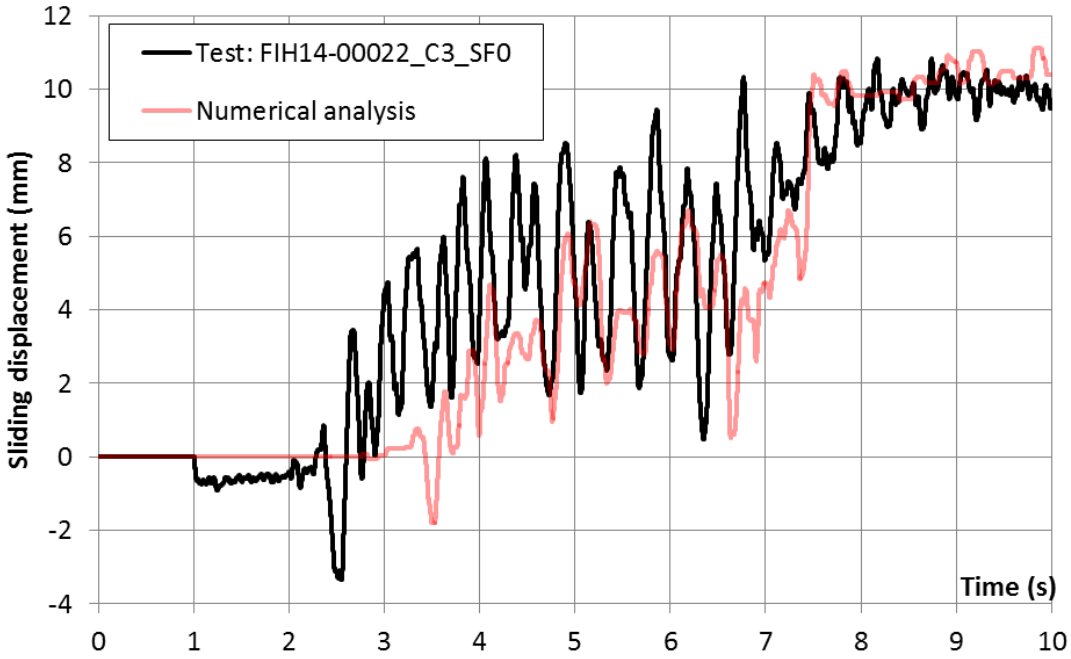

Figure 13. Sliding displacements of Rack1: Experimental vs. numerical

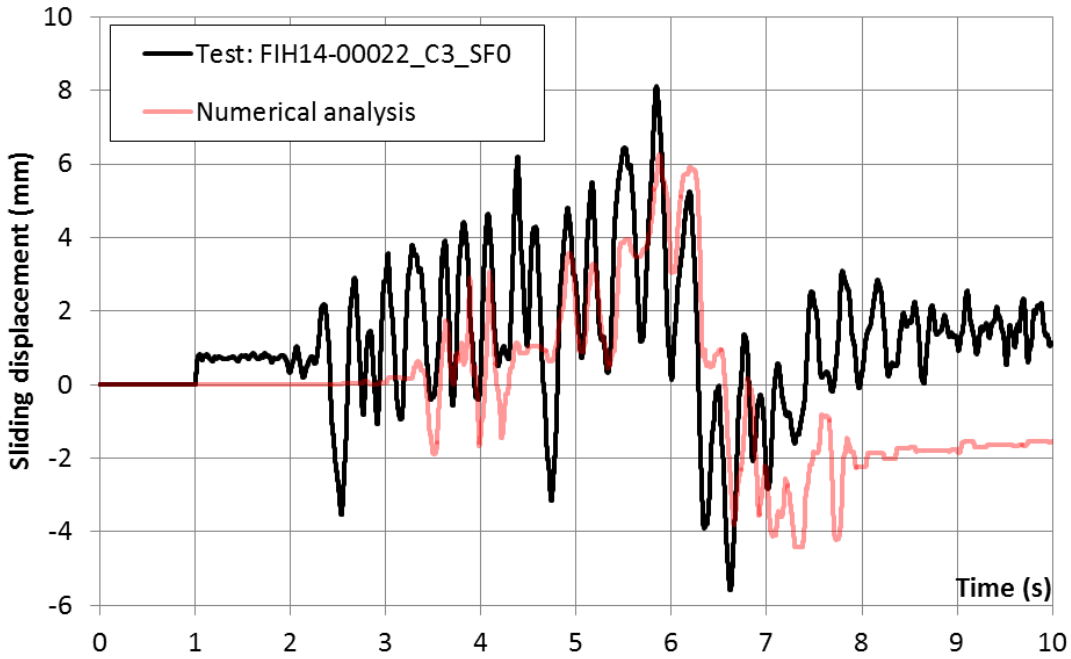

Figure 14. Sliding displacements of Rack2: Experimental vs. numerical

5.3 Vertical forces on support

Experimental and numerical vertical forces on support are also compared. Figure 15 plots both measures at the contact between Rack1 and pool. Experimental records from LC1 are filtered at 70 Hz and tared to set the nominal underwater weight at the initial in agreement with the numerical outputs. Reactions are always positive and the zero values represent liftoff events.

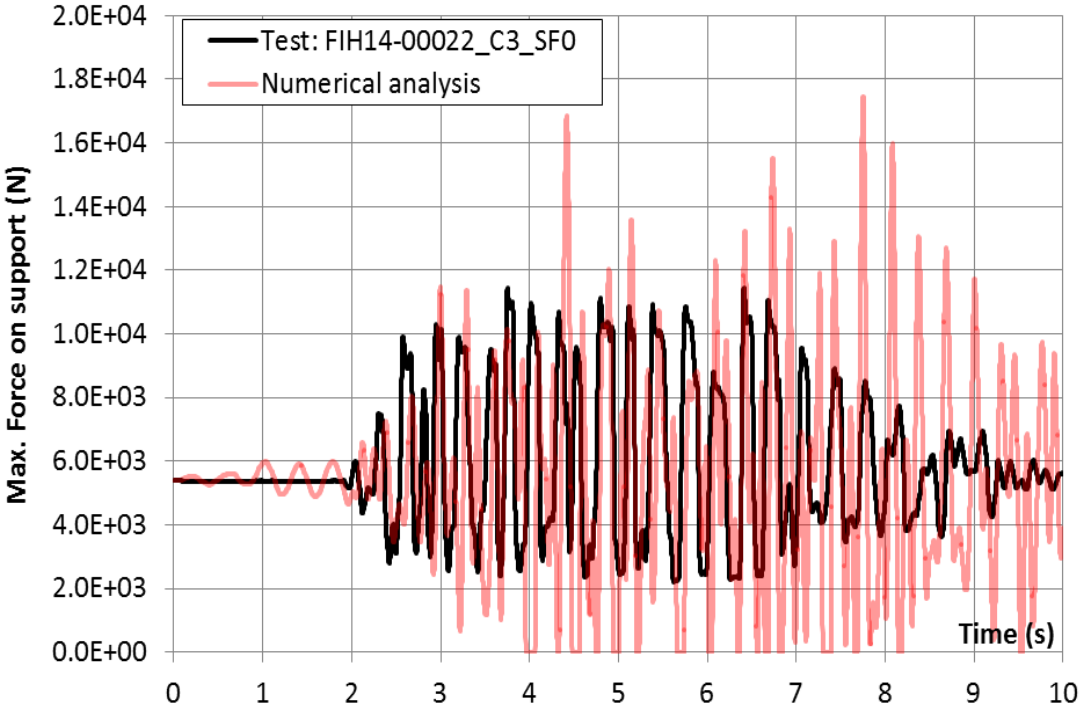

Figure 15. Sliding displacements of Rack2: Experimental vs. numerical

It is highlighted that the numerical signal is more volatile and should also be filtered to reduce the numerical noise prior to analyze the contact impact forces. Nevertheless, numerical analysis returns higher reaction peaks than collected by the test. These peaks are proportional to the stiffness of the elastic contact.

5.4 Hydrodynamic pressures

The hydrodynamic pressures collected in the vibration tests are compared with the average value returned by the numerical analysis. Figures 16, 17 and 18 plot both measures at the external and internal face of the Rack2 and at the pool wall respectively. Although both sources do not perfectly agree, it is worthy to note that the range of variation and the order of magnitude are consistent.

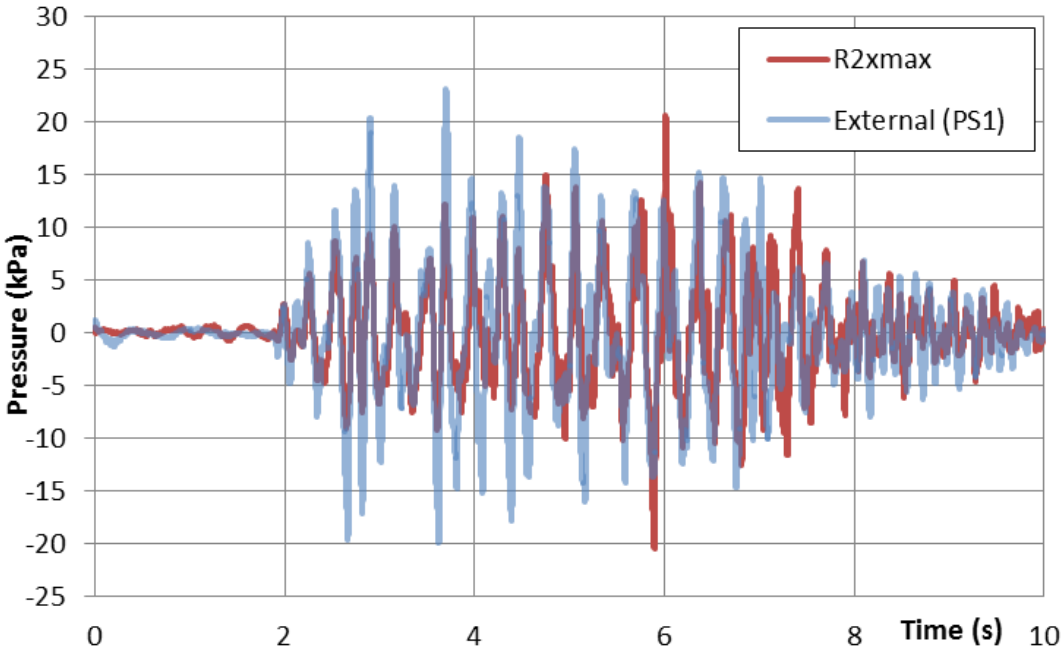

Figure 16. Hydrodynamic pressures at the external face of the Rack2: Experimental vs. numerical

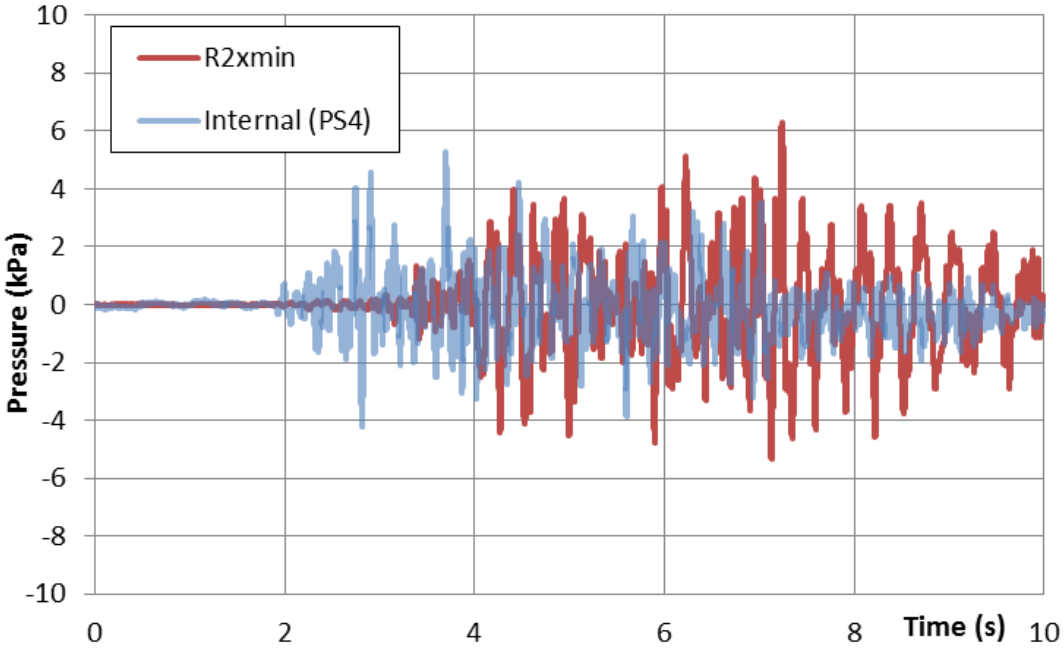

Figure 17. Hydrodynamic pressures at the internal face of the Rack2: Experimental vs. numerical

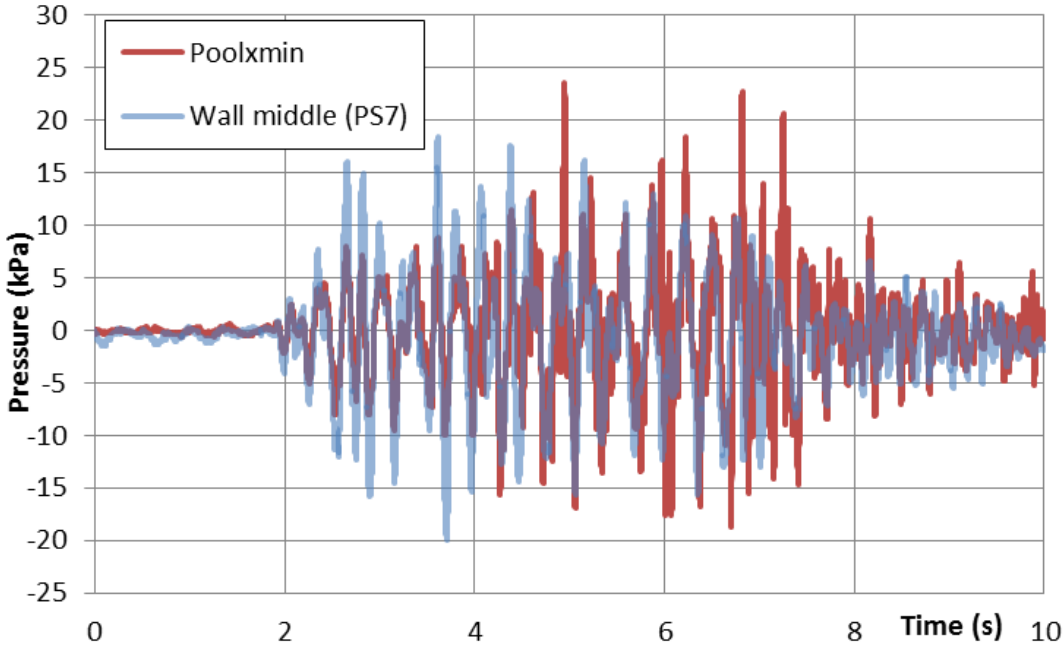

Figure 18. Hydrodynamic pressures at the Pool wall: Experimental vs. numerical

6 Conclusions

This paper describes the vibration tests carried out on a reduced scale 2-rack model and simulates the experimental response through transient implicit integration of an ad-hoc Finite Element model based on the hydrodynamic mass concept. The influence of the velocity reached by the rack units on their sliding displacement is discussed. The water coupling effect between wet surfaces is detailed and the in-phase motion of the free-standing units is highlighted. Both units slide over the pool floor following the cycles of the pool shakings but their respective separation barely evolves. Therefore, hydrodynamic pressures between units remain low compared to the pressures raised at the pool walls. A parabolic pressure distribution is observed over the rack faces. The noticed pressure fall around the rack's top edge is a consequence of the loss of confinement of the water streamlines.

Several numerical simulations are conducted looking for the best modeling and analysis variables to accurately represent the rack seismic problem. However, the sensitive nature of the phenomena makes impossible a perfect recreation between numerical and experimental observations. Divergences cumulate from the beginning and propagate throughout the seismic duration. Fortunately, details are not necessary for a proper rack design and the

focus is on the macroscopic behavior from a quantitative point of view. The unavoidable scatter is considered acceptable as numerical outputs show a good agreement in terms of order of magnitude with the experimental data. It validates the assumptions of the analysis methodology and the adjustments of the Finite Element model.

7 Acknowledgment

This research has received funding from the European Union's Horizon 2020 research and innovation programme under the Marie Skłodowska-Curie grant agreement No. 642453 (http://trussitn.eu). Physical tests are funded by the Spanish Ministry of Economy, Industry and Competitiveness.

8 References

Instituto de Hidraulica ambiental Cantabria, Equipos Nucleares S.A., 2016. 'ANSTER - Almacenamiento Nuclear Seguro Ante TERremotos', (*http://anster.ihcantabria.es/)* Gobierno de España, Ministerio de economía, Industria y Competitividad.

ANSYS, Inc. 2012. ANSYS QA2012-01.

ANSYS, Inc., 2013. ANSYS Mechanical User's guide; Release 15.0

Ashar H, DeGrassi G., 1989. Design and analysis of free-standing spent fuel racks in nuclear power plants (an overview). 10th International conference on Structural Mechanics in Reactor Technology, (SMiRT-10); CONF-890855—43, BNL-NUREG-42667. Anaheim (USA)

Champomier F., Delemontey R., Sollogoub, P., Toumbas D., 1989. Seismic design of a spent fuel storage rack. 10th International conference on Structural Mechanics in Reactor Technology (SMiRT-10). CONF-890855; 589-594. Anaheim (USA)

Champomier F., Peron J.Y., 2001. Seismic justification of free standing spent fuel storage racks: experimental versus computed behaviour. 9th International conference on nuclear engineering (ICONE-9), Nice (France).

Chung H, Chen S., 1984. Hydrodynamic mass. United States Government. CONF-840647—9.

DeGrassi G., 1992. Review of the technical basis and verification of current analysis methods used to predict seismic response of spent fuel storage racks, NUREG/CR-5912, BNL-NUREG-52335.

Fritz R.J., 1972. The effect of liquids on the dynamic motions of immersed solids. Journal of engineering for industry. 167-173

Fujita, K., Tanaka, M., Nakamura, M., Tsujikura Y., 1988. Study of the seismic isolated spent fuel storage rack. 9th World conference on earthquake engineering, Tokyo-Kyoto (Japan)

Fujita, K., Tanaka, M., Nakamura, M., Tsujikura Y., 1990. Seismic testing of the base-isolated PWR spent-fuel storage rack. JSME international Journal, 3;33-3

Gonzalez Merino, A., Costas, L., Gonzalez, A. 2017. Sources of uncertainty in the seismic design of submerged free-standing racks. Energy Procedia. 127:310-319

Gonzalez Merino, A., Costas, L., Gonzalez, A. 2018. Influence of the modelling properties on the seismic response of free-standing spent fuel racks. Nuclear Engineering and Design.

Hilbert H.M., Hughes T.J.R., Taylor R.L., 1977. Improved numerical dissipation for time integration algorithms in structural dynamics. Earthquake engineering and structural dynamics;5:283-292.

Hinderks M, Ungoreit H, Kremer G., 2001. Improved method to demonstrate the structural integrity of high density fuel storage racks. Nuclear Engineering and Design. 206:177-184.

Housner G.W:,1963. The dynamic behaviour of water tanks. Bulletin of the seismological society of America. 53,2:381-387.

Iwasaki A., Nekomoto Y., Morita H., Kishimoto Y., Taniguchi K., Takaki Y., 2016. Development of free-standing rack seismic evaluation. Mitsubishi Heavy Industries Technical Review. 53,2:103-107

Iwasaki A., Nekomoto Y., Morita H., Taniguchi K., Okuno D., Matsuoka T., Chigusa N., 2012 (a). Experimental study on free standing rack loading full fuel assembly. ASME Pressure Vessels and piping conference PVP2012-78458, Toronto (Canada)

Iwasaki A., Nekomoto Y., Morita H., Taniguchi K., Okuno D., Matsuoka T., Chigusa N., 2012 (b). Experimental parameter study on free standing rack. ASME Pressure Vessels and piping conference PVP2012-78451, Toronto (Canada)

Iwasaki A., Nekomoto Y., Morita H., Taniguchi K., Okuno D., Matsuoka T., Chigusa N., 2012 (c). Analysis study on free standing rack under the earthquake excitation. ASME Pressure Vessels and piping conference PVP2012-78462, Toronto (Canada)

Iwasaki A., Nekomoto Y., Morita H., Taniguchi K., Okuno D., Matsuoka T., Chigusa N., 2013. Development of seismic design method for free standing rack. ASME Pressure Vessels and piping conference PVP2013-97168, Paris (France)

Kaneko S., Shirai H., 2015. Construction of dynamic model for free standing spent fuel rack under seismic excitation. Pressure Vessels and piping conference PVP2015-45069, Boston (USA)

Lee GM, Kim KS, Park KB, Park JK, Three-dimensional seismic analysis for spent fuel storage rack. Journal of the Korean Nuclear Society 1998; 30:91-98

Liu Y., Lu D. Liu H., Huang Y., 2018. The shaking table experiments on sliding and overturning of CAP1400 spent fuel storage rack with the effect of FSI. Annals of Nuclear energy 112; 277-288.

Liu Y., Lu D. Wuang Y., Liu H., 2016. The sliding and overturning analysis of spent fuel storage rack based on dynamic analysis mode. Science and technology of nuclear installation. 8368504

Moudrik R, Queval J.C, Gantenbein F., Champomier F., Trollat C. 1995. Test and calculations on a scale one spent fuel storage rack. Conference on structural mechanics in reactor technology (SMIRT-13) Porto Alegre (Brazil).

Newmark N., 1959. A method of computation for structural dynamics. Journal of the engineering mechanics division. 67-95.

Queval J.C:, Sollogoub P., Champomier F., Vallat S. 1999. Seismic behaviour of spent fuel storage racks. Conference on structural mechanics in reactor technology (SMIRT-15) Seoul (Korea).

Ren M., Stabel J., Comparison of different analytical formulation for FSI between fuel storage racks. International conference on structural mechanics in reactor technology (SMiRT-15). Seoul (Korea)

Sakamoto K., Kan R., Takai A., Kaneko S., 2017. Construction of dynamic model of planar and rocking motion for free standing spent fuel rack. ASME pressure vessels and Piping Conference PVP2017-65172, Hawaii (USA)

Soler, A., Singh K.P. 1984. Seismic response of a free standing fuel rack construction to 3-D floor motion. Nuclear engineering and Design, 80, 315-329.

Soler, A.I., Singh, K.P. 1982. Dynamic coupling in a closely spaced two-body system vibrating in a liquid medium: the case of fuel racks, 3rd Keswick International conference in nuclear plants.

Stabel J. M. Ren, Swelim H. 1993. Calculation of seismic loads on fuel storage racks under consideration of fluid-structure interaction. International conference on structural mechanics in reactor technology (SMIRT-12). Stuttgart (Germany)

Stabel J. M. Ren,. 2001. Fluid-structure-interaction for the analysis of the dynamics of fuel storage racks in the case of seismic loads. Nuclear Engineering and Design. 206:167-176

Stevenson J.D., 1980. Structural damping values as a function of dynamic response stress and deformation levels. Nuclear Engineering and Design 60:211-237

Takaki Y., Katsuhiko T., Kishimoto J., Iwasaki A., Nekomoto Y., Kuga T., Kameyama M., 2017. Seismic design of free standing racks in Japanese nuclear power plants. ASME Pressure Vessels and piping conference PVP2017-65740 Hawaii (USA)

U.S. Nuclear Regulatory Commission. 1978. OT position for review and acceptance of spent fuel storage and handling applications. Amended by NRC letter in 1979

U.S. Nuclear Regulatory Commission. 1981. Standard Review Plan for the review of safety analysis reports for nuclear power plants. Chapter 3– Design of structures, components, equipment and systems. NUREG-0800, formerly issued as NUREG-75/087.

Zhao Y, Wilson PR, Stevenson JD. 1996. Nonlinear 3-D dynamic time history analysis in the reracking modification for a nuclear power plant. Nuclear Engineering and Design. 165:199-221.

Zhao Y., 1997. Finite element modelling and analysis of nonlinear impact and frictional motion response including fluid-structure coupling effects. Shock and vibration. 4:311-325.